Check for updates

Bistable magnetic valves for selective sweat sampling in wearable microfluidics†

Chaemin Kim, [iD] [a] Chanyong Shin, [b] Anna Lee, [iD] *[a]
Jonghyun Ha [iD] *[b] and Jungil Choi [iD] *[b]

Selective sweat sampling with high spatial and temporal resolution remains a key challenge in wearable microfluidic systems for biochemical monitoring. Here, we present a skin-conformal microfluidic platform that enables targeted, chamber-specific sweat collection by integrating bistable, magneto-active elastomeric valves. Each valve is toggled between open and closed states using a simple external magnetic field, requiring no continuous power. The bistable design provides mechanical memory, maintaining valve states without sustained actuation, and thus allows highly energy-efficient fluid control. By embedding magnetic particles in a shell structure with geometric bistability, we achieve reliable magnetic actuation and characterize the critical pressures associated with valve switching under varying magnetic flux densities. These results demonstrate the feasibility of using the system for practical, localized sweat collection and suggest its utility in wearable sensing applications that require spatially discrete and contamination-free sampling.

1 Introduction

Wearable sensors provide a powerful means for continuous, non-invasive monitoring of physiological states, enabling real-time health tracking and personalized healthcare applications.[1–3] Among various sensing approaches, sweat-based analysis is particularly promising because sweat is naturally secreted without requiring active stimulation and contains diverse biomarkers—including electrolytes, metabolites, and hormones—that reflect systemic physiology.[4–6] Importantly, sweat composition dynamically evolves over time in response to physiological changes such as hydration status, metabolic activity, and stress levels,[7] making time-resolved sampling essential for accurately capturing dynamic biomarker profiles. As a result, sweat-based wearable sensors have been developed for applications such as monitoring hydration, electrolyte balance, and stress levels in real time.[8–11]

Recent advances in microfluidic-based sweat sensors have focused on leveraging passive fluid transport mechanisms such as capillary forces or surface energy gradients.[12–14] These systems enable power-free operation and compatibility with skin-mounted wearables, but they generally collect sweat continuously once secretion begins.[15–18] As a result, conventional designs struggle to isolate temporally distinct sweat samples and often suffer from cross-contamination between analyte-rich regions.[19,20] Several prior works have attempted to enable sequential sweat collection by employing compartmentalized microfluidic channels, gated flow mechanisms, or moisture-responsive hydrogels as passive valves.[21–24] Thus, realizing truly programmable, reconfigurable, and independent fluid control for multi-chamber sweat sampling remains a critical challenge.[25–27] In particular, previous user-controlled systems based on mechanical input have demonstrated resettable or on-demand collection capabilities,[28–31] but still face limitations in continuous programmability, spatial resolution, or energy efficiency.

Here, we present a skin-mounted sweat collection device that integrates magneto-active bistable valves for discrete, chamber-specific sampling. Each valve consists of a bistable shell structure embedded with magnetic particles, which can be reversibly toggled between stable open and closed states *via* magnetic actuation and mechanical indentation. Bistable shells are thin-walled structures that exhibit two mechanically stable configurations determined by their geometric parameters, enabling snap-through transitions and mechanical memory.[32–36] By leveraging reprogrammable

[a] Department of Mechanical Engineering, Pohang University of Science and Technology (POSTECH), 77 Cheongam-ro, Nam-gu, Pohang 37673, Republic of Korea. E-mail: annalee@postech.ac.kr; Tel: +82 54 279 2176
[b] Department of Mechanical Engineering, Ajou University, 206 World cup-ro, Yeongtong-gu, Suwon 16499, Republic of Korea. E-mail: hajh@ajou.ac.kr, cji@ajou.ac.kr; Tel: +82 31 219 2344, +82 31 219 2343
† Electronic supplementary information (ESI) available. See DOI: https://doi.org/10.1039/d5lc00576k

magnetic responsiveness, mechanical bistability, and passive state retention, this system allows precise temporal control over sweat collection while maintaining low-power operation and simple device architecture. This approach offers a versatile platform for reliable, repeatable, and reprogrammable sweat sampling under real-world conditions, advancing the capabilities of wearable sweat-sensing technologies for longitudinal biochemical monitoring.

2 Design and working principle

We develop a wearable sweat collection device capable of selectively collecting sweat in designated chambers by independently controlling the opening and closing of each valve. As illustrated in Fig. 1a, the device consists of three functional layers: a i) magneto-active valve layer, a ii) microfluidic platform layer, and an iii) adhesive layer.

Each layer plays a distinct role in facilitating the selective collection of sweat. The top layer, i) magneto-active valve layer, contains valves based on a bistable shell structure that switches between stable open and closed states. In its undeformed (pristine) state, the shell leaves the fluidic path unobstructed, allowing sweat to flow into the valve chamber. Upon inversion, the shell seals the path and blocks further flow (Fig. 1b). This layer also includes outlet holes that release excess sweat, preventing fluid buildup and minimizing backward pressure—flow resistance that opposes forward transport of sweat through the microchannel network. The middle layer, ii) microfluidic platform layer, comprises microfluidic channels, valve chambers, and collection chambers. An inlet hole allows sweat to enter from the skin surface, as indicated by the yellow arrows in Fig. 1a. The channels guide sweat to the valve chamber, where its passage is regulated. The microfluidic channels have a width
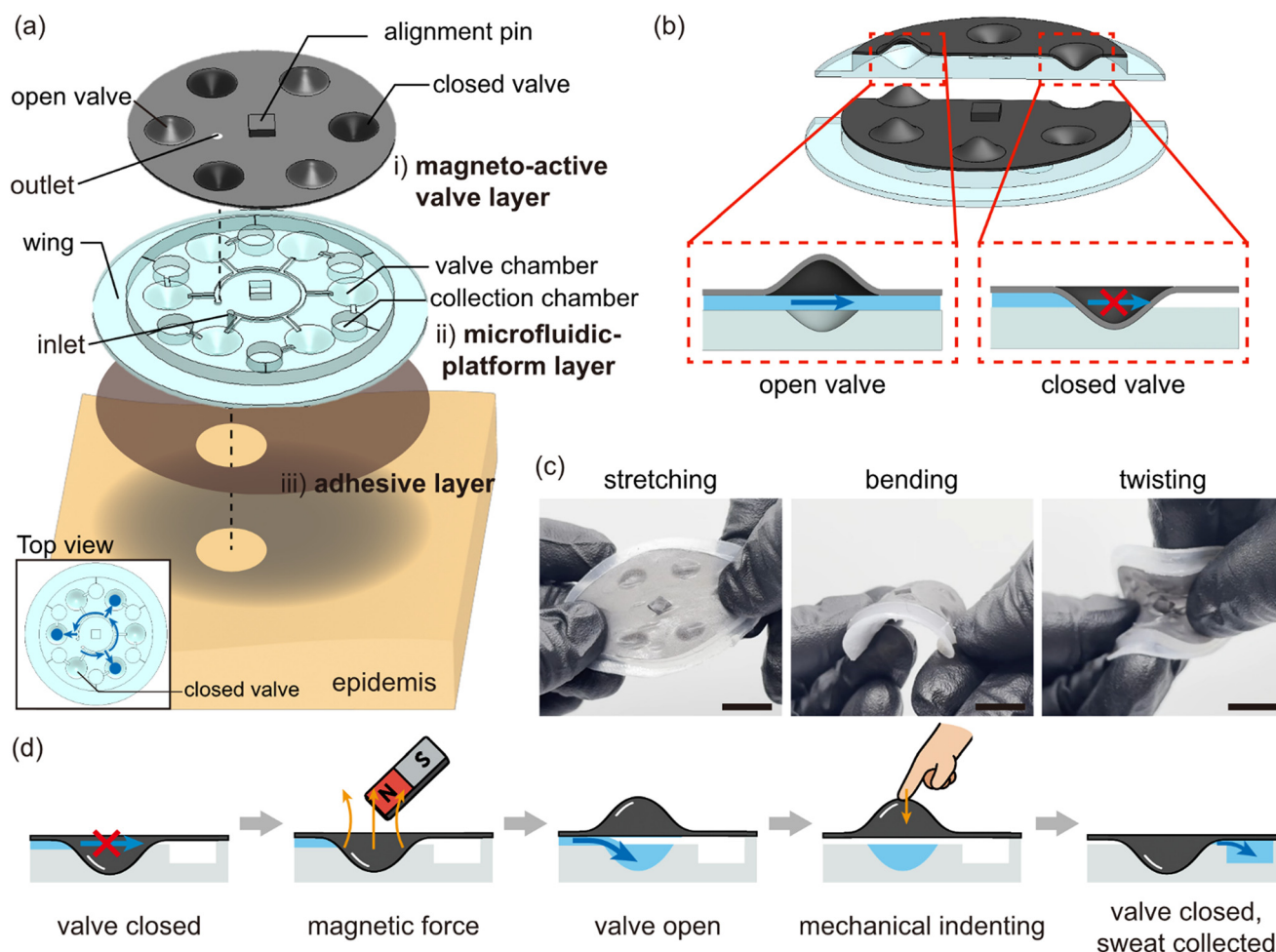

Fig. 1 Schematic illustration of the magneto-active sweat collection device. (a) An exploded view shows the three-layered architecture: i) magneto-active valve layer, ii) microfluidic platform layer with inlet hole and fluidic chambers, and iii) adhesive layer for skin attachment. The magneto-active valves have a circular geometry with a radius of 3 mm. Blue arrows in the top view image indicate the direction of sweat flow. As seen in the top view, sweat selectively enters only the valve chambers of the opened valves, while no fluid enters the closed valves. (b) Working principle of the bistable valve: the undeformed (open) state allows fluid to enter the valve chamber, while the inverted (closed) state blocks the channel. (c) Demonstration of mechanical deformability under stretching, bending, and twisting, enabled by soft elastomeric materials. All scale bars, 10 mm. (d) Sequential operation of selective sweat collection: magnetic opening of the valve, accumulation of sweat in the valve chamber, mechanical indentation to close the valve, and directed transfer of sweat to the collection chamber.

of 600 μm and a height of 300 μm, while each collection chamber has a diameter of 4.3 mm and a depth of 1.5 mm. The maximum capacity of each collection chamber is approximately 22 μL. We use alignment pins during bonding to ensure precise alignment between the valve and channel features. The bottom layer, iii) adhesive layer, consists of a soft adhesive film that enables conformal attachment to the skin. All layers are composed of soft, stretchable materials, allowing the device to maintain functional integrity under stretching, bending, and twisting, as demonstrated in Fig. 1c.

The bistable valve enables reversible control of fluid flow through magnetically and mechanically induced deformation. In the closed state, the bistable shell obstructs the channel, preventing sweat from entering the valve chamber. When an external magnet approaches, magnetic attraction causes the shell to deform upward, triggering a snap-through transition to the open state (Videos S1 and S2†). The shell remains in the open state even after the magnet is removed due to its bistable mechanical nature, allowing sweat to accumulate in the valve chamber. To transfer the collected fluid, we apply mechanical indentation to return the shell to its closed configuration. This action pushes the stored sweat past the valve and into the adjacent collection chamber, while resealing the valve to prevent cross-contamination. By selectively actuating individual valves in this manner, sweat is directed into designated chambers without mixing between regions, as schematically shown in Fig. 1d.

The bistable valve enables reversible control of fluid flow through magnetically and mechanically induced deformation. In the closed state, the bistable shell obstructs the channel, preventing sweat from entering the valve chamber. When an external magnet approaches, magnetic attraction causes the shell to deform upward, triggering a snap-through transition to the open state (Videos S1 and S2†). The shell remains in the open state even after the magnet is removed due to its bistable mechanical nature, allowing sweat to accumulate in the valve chamber. As demonstrated in Video S2,† valve activation only occurs when the magnet is precisely aligned with the valve. Slight misalignment or increased distance fails to trigger the transition, highlighting the spatial selectivity and robustness of the magnetic actuation mechanism. To transfer the collected fluid, we apply mechanical indentation to return the shell to its closed configuration. This action pushes the stored sweat past the valve and into the adjacent collection chamber, while resealing the valve to prevent cross-contamination. By selectively actuating individual valves in this manner, sweat is directed into designated chambers without mixing between regions, as schematically shown in Fig. 1d.

3 Experimental methods

3.1 Materials

We fabricate the magneto-active valve layer using a vinyl polysiloxane elastomer (Elite Double 8, Zhermack S.p.A.,

Italy) as the matrix. Hard magnetic neodymium–iron–boron (NdFeB) particles (MQP-S-11-9, Neo Magnequench Korea Co., Republic of Korea) are incorporated as magnetic particles. For the microfluidic platform layer, we use a platinum-cured silicone elastomer (Ecoflex™ 00-30, Smooth-On, USA). We use deionized water (DI water) for *in vitro* testing and collect human sweat for on-body experiments. To improve visual contrast in the images, we add dye to the DI water.

We fabricate molds using a 3D printer (Form 4, Formlabs Inc., USA) with a clear photopolymer resin (RS-F2-GPCL-04, Formlabs Inc., USA), offering a layer height resolution of 25 μm.

3.2 Fabrication of the magneto-active valve and microfluidic platform layers

We define the shell geometry using a parameterized polynomial profile that produces rotationally symmetric structures suitable for bistable behavior. We adopt a bistable shell design introduced by Brinkmeyer *et al.*[32] The shell profile is defined as

$$y = L[1 + 2(x/R)^3 - 3(x/R)^2], \, x \in [0, R],$$

and we revolve this profile about the *y*-axis to form a rotationally symmetric shell with a third-order polynomial contour. Here, L is the shell height, R is the shell radius, and T is the shell thickness. We note that the shell does not inherently exhibit bistability; rather, bistable behavior
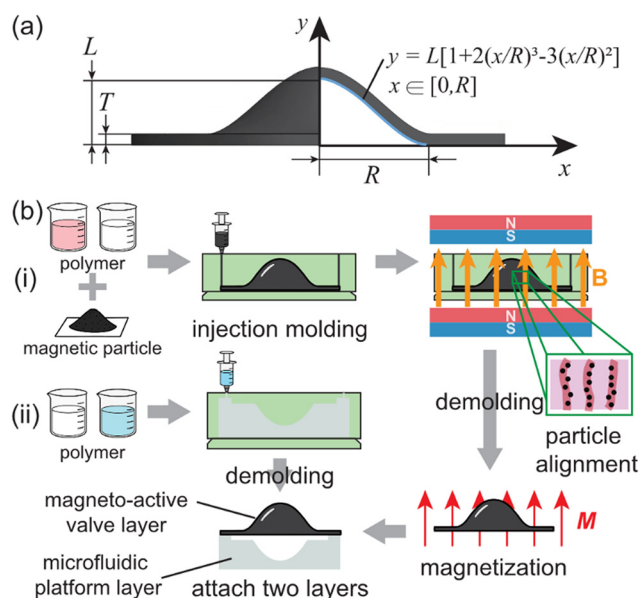

Fig. 2 (a) Geometry of the bistable shell used as the valve structure. The profile, defined by a cubic polynomial, is revolved around the *y*-axis to generate an axisymmetric bistable shell. (b) Fabrication process of the magneto-active sweat collection device. (i) The magneto-active valve layer and (ii) the microfluidic platform layer are individually molded, aligned, and bonded to complete the device. To induce directional particle alignment, the magnetic elastomer is cured while the mold is placed between permanent magnets, causing the embedded NdFeB particles to align along the magnetic field lines.

emerges depending on the geometric parameters, particularly the ratios T/R and L/R. In our design, we use $T/R = 0.1$, $R = 3$ mm, and $L = 1.77$ mm, which fall within the bistable regime identified in previous studies[32] (Fig. 2a).

We fabricate the magneto-active valve layer by mixing NdFeB particles into an elastomer matrix and controlling their alignment during the curing process. We prepare composites with particle concentrations of 10, 30, 50, and 70 wt%, inject the uncured mixture into 3D-printed molds, and apply one of two curing conditions: (1) randomly dispersed, where the composite is cured at room temperature without an external magnetic field, and (2) aligned, where the mold is placed between two parallel permanent magnets to align the particles along the field lines (Fig. 2b-i). Under a uniform magnetic field $\mathbf{B}$, each NdFeB particle acquires a magnetic moment $\mathbf{m}$, and the particle aligns to minimize the magnetic potential energy, given by $U_{\mathrm{m}} = -\mathbf{m} \cdot \mathbf{B}$, with bold-face symbols indicating vectors. This alignment is further stabilized by dipole–dipole interactions that favor a head-to-tail configuration. Because the matrix remains fluid prior to curing, particles can rotate and migrate, forming anisotropic microstructures that are fixed upon solidification.[37–40] After curing, we demold both *randomly dispersed* and *aligned* samples and magnetize them using a magnetizer (MCB-3530, SCMI Co., Republic of Korea) to ensure consistent remanent magnetization across all samples for subsequent actuation testing. While pre-magnetized NdFeB particles have been used in other applications such as printed self-healing devices,[41] our post-curing magnetization approach avoids agglomeration and ensures uniform particle distribution. We then punch each valve layer using a 1 mm diameter punch to form outlet holes for sweat release.

The microfluidic platform layer incorporates microfluidic channels, valve chambers, and collection chambers designed to regulate sweat flow and store collected fluid. We fabricate this layer by casting Ecoflex into a 3D-printed mold. After full curing, we punch a 2 mm diameter inlet hole into the layer (Fig. 2b-ii). To assemble the sweat collection device, we demold the microfluidic platform layer at 90% cure and place it onto the valve layer. Alignment pins are used to ensure precise registration between the two layers.

3.3 Evaluation of particle alignment and material properties

We characterize particle alignment by analyzing microstructure and optical transmittance using imaging-based techniques. We observe the microstructure of aligned particles by examining surface morphology using a field-emission scanning electron microscope (FE-SEM; JSM-IT710HR, JEOL Ltd., Japan) operated at 5 kV. To prevent charging, we sputter-coat samples with a thin layer of platinum. We measure optical transmittance by placing 300 μm-thick membranes on transparent acrylic plates and imaging them with a mirrorless digital camera (ZV-E10, Sony Corporation, Japan) under uniform lighting. We define the reference intensity as the grayscale value of the bare acrylic surface (representing 100% transmittance), and normalize the mean grayscale intensity of each sample region to this reference using ImageJ (NIH, USA).

We investigate the functional response of the composite with respect to particle alignment and concentration. Magnetic hysteresis measurements are conducted to quantify the remanent magnetization of both randomly dispersed and aligned samples containing 10, 30, 50, and 70 wt% of magnetic particles. These measurements are performed using a vibrating sample magnetometer (VSM; Model 7404, Lake Shore Cryotronics Inc., USA) under an applied magnetic field range of ±10.0 kOe. To evaluate mechanical performance, uniaxial compression tests are carried out using a universal testing machine (Instron 3343, Instron Corp., USA). Cuboid specimens (12.7 mm × 12.7 mm × 25.4 mm) are tested in accordance with the ASTM D695 standard at a strain rate of 1 mm min^{-1}.

3.4 Experimental setup for valve actuation and fluid control

We apply a controlled magnetic field using a Helmholtz coil pair (Helmholtz Pair of Coils S, 3B Scientific GmbH, Germany), with current supplied by a DC power supply (FTP1180-60-60, FaithTech, Canada). We define the current direction such that rents are used to reverse the magnetic field direction. We monitor the magnetic field intensity using a 3-axis magnetic field sensor (GDX-3MG, Vernier Software & Technology, USA).

We evaluate valve sealing and opening performance by injecting DI water through the microfluidic channel using a pressure-based flow controller (Flow EZ™ 2000 mbar, Fluigent SA, France). Valve integrity is evaluated by applying a constant back pressure and monitoring for fluid leakage over a test duration of up to 600 seconds. Fluid flow at the outlet is monitored in real time using a liquid flow sensor (SLF3S-0600F, Sensirion AG, Switzerland), connected to a PC *via* SCC1-USB and visualized using Sensor viewer software. The pressure at which continuous flow is first observed is defined as the leaking pressure.

4 Results and discussion

4.1 Effect of particle concentration and alignment on material properties

We examine the particle alignment in magneto-active elastomers using SEM. Samples are prepared with particle concentrations of 10, 30, 50, and 70 wt%. In aligned samples, which we cure between two parallel permanent magnets, particles orient along the magnetic field direction (Fig. 3a). In contrast, randomly dispersed samples, cured without a magnetic field, exhibit uniform, isotropic particle distribution. These observations confirm that NdFeB particles align effectively when exposed to a magnetic field during curing.

We evaluate the optical transmittance of the elastomer membranes as a function of particle concentration and alignment (Fig. 3b). NdFeB powder is black and optically
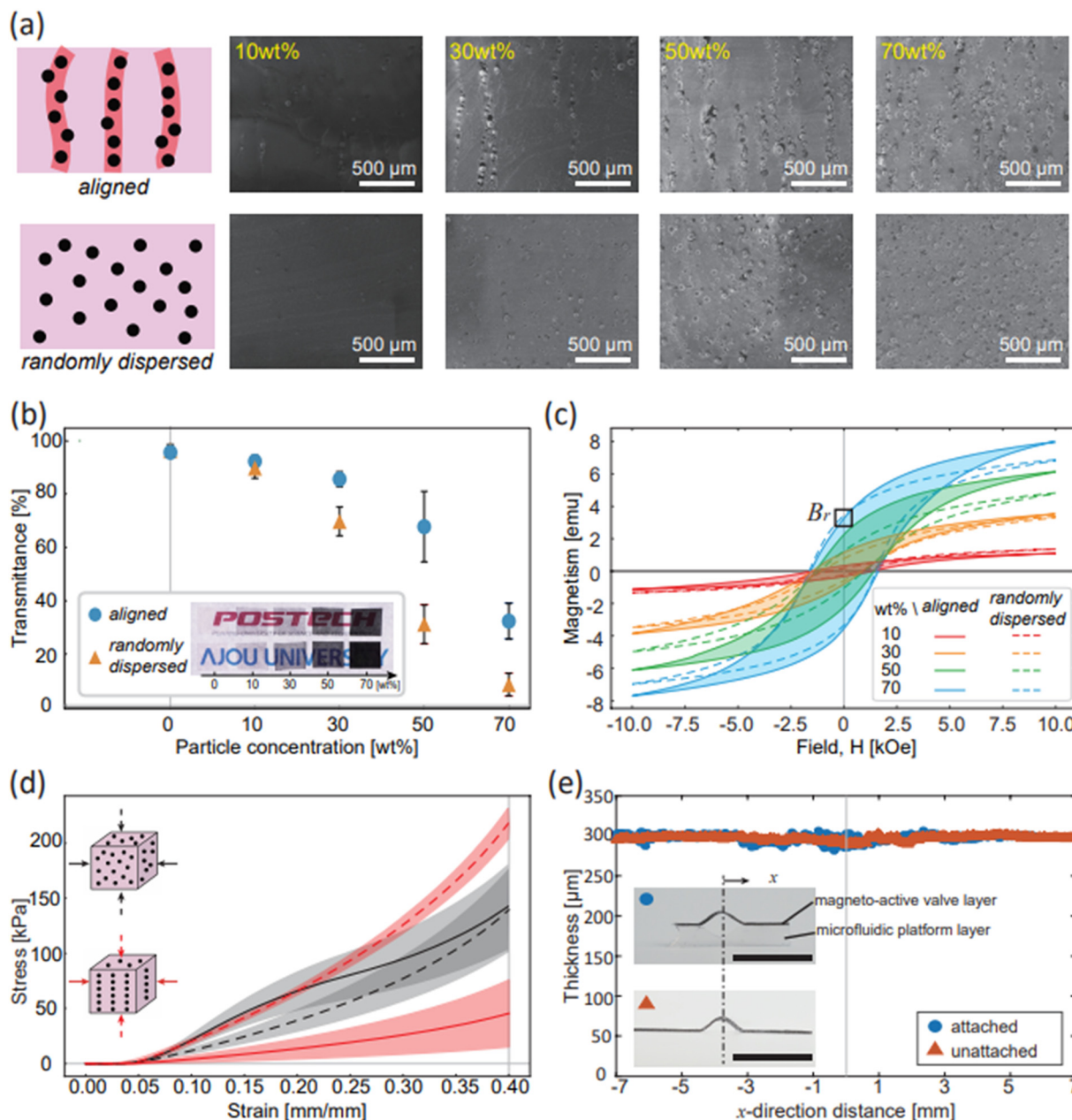
Fig. 3 Characterization of magneto-active elastomers with varying particle alignment. (a) SEM images of magneto-active elastomers with various particle concentrations. *Aligned* samples (top) show particle orientation along the magnetic field direction, while *randomly dispersed* samples (bottom) exhibit isotropic distribution. (b) Optical transmittance of elastomer membranes as a function of particle concentration and alignment. *Aligned* samples exhibit improved transmittance due to reduced light scattering. (c) Remanent magnetization (B_r) extracted from hysteresis curves at $H = 0$, showing higher values in *aligned* samples. (d) Directional compressive modulus of composites with 50 wt% NdFeB. *Aligned* samples exhibit mechanical anisotropy. (e) A thickness comparison of the magneto-active valve layer before and after attachment of the microfluidic platform layer confirms successful integration. Scale bars represent 10 mm.

opaque, while the elastomer matrix is highly transparent. Using an acrylic plate as a reference with 100% transmittance, we find that a neat elastomer film without particles shows a high baseline transmittance. Compared to randomly dispersed samples, aligned samples consistently exhibit higher transmittance across all concentrations. This enhancement is attributed to reduced light scattering, as alignment minimizes refractive index mismatch and

structural irregularities.[42,43] While increasing the particle concentration typically improves magnetic response, the data in Fig. 3b reveal a significant drop in performance gain beyond 50 wt%. This inflection point indicates diminishing returns at 70 wt%, justifying the selection of 50 wt% as the optimal composition.

We measure the remanent magnetization (B_r) of the composites to assess how particle alignment and concentration

influence their magnetic response (Fig. 3c). B_r represents the residual magnetization retained after the external magnetic field is removed, indicating the material's ability to remain magnetized without continuous stimulation. Compared to randomly dispersed samples, aligned samples consistently exhibit higher B_r due to the coherent orientation of individual particle magnetizations. Each NdFeB particle inherently possesses a strong magnetic moment. After curing, we magnetize all samples using a uniform external magnetic field applied along the y-axis. As a result, the remanent magnetization B_r is defined as $B_r\hat{y}$, independent of the particle alignment within the matrix. When these moments are physically aligned within the elastomer matrix, they add constructively to produce greater net remanence. In contrast, randomly dispersed arrangements lead to partial cancellation of magnetic vectors, resulting in a lower overall B_r. As highlighted by the shaded regions in Fig. 3c, aligned and high-concentration samples exhibit hysteresis loops that cover a wider range of magnetic field and magnetization, indicating greater magnetic energy storage and dissipation per cycle. This broader loop reflects stronger dipolar interactions and enhanced magnetic stability—key factors for reliable actuation and memory-like behavior. These results demonstrate that the spatial orientation and density of hard magnetic particles are critical for tuning the magnetic performance of magneto-active elastomers.

We characterize the mechanical response of composites with 50 wt% NdFeB using directional compression tests (Fig. 3d). Randomly dispersed samples show isotropic compressive modulus in all directions due to uniform particle distribution. In contrast, aligned samples exhibit pronounced mechanical anisotropy. The modulus measured perpendicular to the alignment (in-plane) is significantly higher than that measured parallel to the alignment (out-of-plane). This anisotropy arises from the microstructural arrangement in which in-plane alignment restricts lateral deformation and forms a load-bearing network. In contrast, along the alignment axis, the deformation is governed primarily by the matrix itself, and interfacial slippage between particles and matrix can reduce the effective stiffness. This directional anisotropy was intentionally incorporated into the valve design to enhance bistable stability. The alignment-induced increase in stiffness is expected to contribute to more robust snap-through behavior by requiring higher actuation forces and stabilizing the two equilibrium states. In this way, particle alignment serves not only to improve magnetic responsiveness but also to reinforce the mechanical performance of the bistable architecture.

Based on the enhanced magnetic and mechanical properties, we use the aligned sample with 50 wt% NdFeB to fabricate the magneto-active valve layer. This 300 μm-thick layer is bonded to the microfluidic platform layer to complete device assembly. Because the valve relies on a bistable geometry to achieve reversible actuation, preserving its structural form during integration is critical. As shown in Fig. 3e, the valve layer retains its original thickness after bonding, indicating that the bistable architecture remains mechanically intact. This confirms that the integration process does not compromise the structural function of the valve.

4.2 Unit magneto-active bistable valve

We evaluate the magnetic actuation characteristics of a unit magneto-active bistable valve and find that the required external magnetic field for valve opening varies with particle concentration and alignment. As established in section 4.1, both parameters influence the remanent magnetization ($B_r\hat{y}$) of the composite. When we apply an external magnetic field **B** using a custom Helmholtz coil setup, the valve experiences a magnetic torque given by $\boldsymbol{\tau} = \mathbf{m} \times \mathbf{B}$, where the magnetic moment **m** is defined as $\mathbf{m} = (B_r\hat{y}/\mu_0)\cdot V$. Here, V is the volume of the magneto-active region and μ_0 is the vacuum permeability.[44] The direction of $B_r\hat{y}$ reflects the initial magnetization of the valve in its undeformed configuration, where magnetic particles are predominantly aligned along the z-axis. Although the external field **B** is also applied along the z-axis, the valve body undergoes geometric deformation during bistable switching. As a result, **m** and **B** are no longer collinear in the deformed geometry, and their cross product yields a nonzero torque. This deformation-dependent misalignment enables magnetic torque generation even under uniform magnetic fields, providing the driving mechanism for snap-through actuation in the closed state.

As the magnetic moment **m** increases with stronger remanent magnetization, a lower external magnetic field **B** is sufficient to generate the torque required for snap-through actuation. This trend is observed in Fig. 4a, where valves with higher B_r actuate at reduced field strengths. Since B_r itself increases with both particle concentration and alignment (section 4.1), samples with aligned particles require lower actuation fields than those with randomly dispersed ones, even at the same concentration. These results confirm that particle alignment and concentration both enhance magnetic responsiveness and reduce the energetic threshold for valve operation.

We further investigate whether the valve's sealing performance can be modulated in real-time through magnetic input. A valve with 50 wt% NdFeB particles is placed at the center of a Helmholtz coil pair and subjected to varying currents of −20, −10, 0, 10 and 20 A (Fig. 4b). The coil geometry—radius r, turn count n, and separation z—ensures a uniform magnetic field at the center, described by $\mathbf{B} = \mu_0 n I r^2/[r^2 + (z/2)^2]^{3/2}\hat{y}$. By reversing the current polarity, we modulate the torque direction: negative currents reinforce the sealed state, while positive currents promote valve opening.

As shown in Fig. 4b, the magnetic field direction plays a critical role in regulating valve behavior. When the applied field opposes the natural snapping direction of the valve (*i.e.*, negative current), the magnetic torque resists actuation, allowing the valve to remain sealed even under a 15 mbar inlet pressure for over 600 seconds. In contrast, when the field
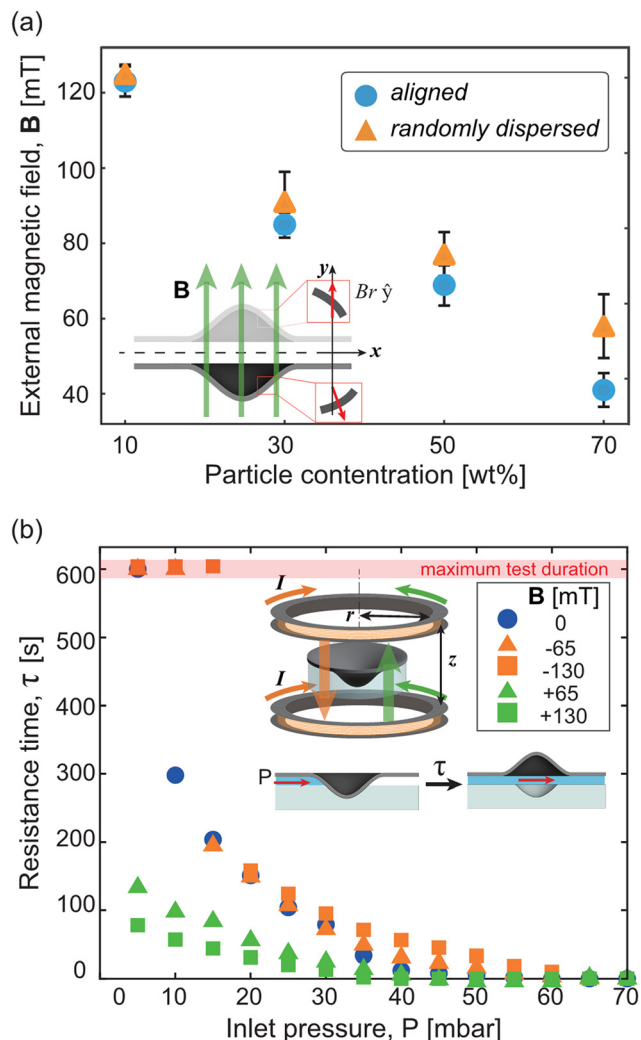
Fig. 4 (a) An external magnetic field is required to actuate the valve, depending on particle concentration and alignment. Valves with higher remanent magnetization exhibit higher actuation thresholds. (b) Resistance time under constant inlet pressure as a function of applied current. Negative currents (orange) enhance valve sealing, while positive currents (green) promote opening.

magneto-active bistable valves. Six unit valves are integrated in front of corresponding collection chambers, allowing individual magnetic actuation to guide incoming liquid into selected chambers. When a valve is opened *via* magnetic actuation, liquid enters only the associated valve chamber. After sufficient accumulation, mechanical indentation is applied to close the valve and transfer the liquid to the adjacent collection chamber (Fig. 1d). Importantly, other chambers remain isolated during this process due to the bistable valve structure, which physically blocks fluid entry when in the closed state. The shell retains this closed configuration without external power, preventing backflow or unintended routing of liquid into non-targeted chambers.

By repeating this open–close sequence in a counterclockwise order, we demonstrate that liquid consistently enters only the chamber linked to the currently open valve (Fig. 5a, Video S3†). Even when new liquid is introduced after a valve has been closed, previously collected liquid remains contained, confirming that the bistable valve mechanism effectively prevents backflow and cross-contamination. This was further validated by sequentially introducing six differently colored liquids, where the extracted liquid from each chamber retained its original color without any evidence of mixing (Fig. S1†). These results validate the system's ability to selectively and temporally control liquid collection.

To assess sample retrieval, a separate test is conducted where sweat is collected across all six chambers, as shown in Fig. 5b. To facilitate visual distinction between chambers, colored dyes are introduced into each collector. After on-body collection, the stored sweat is extracted by inserting a needle into each chamber and applying suction. The recovered sweat is then transferred into separate collection tubes, demonstrating reliable physical separation and uncontaminated retrieval from each chamber.

To further evaluate device performance under physiological conditions, we conducted on-body experiments. All experiments were performed in accordance with the guidelines of institutional review board of Ajou University (202410-HS-002), and experiments were approved by the ethics committee at Ajou University. Informed consents were obtained from human participants of this study. The device is attached to the inner forearm, and sweat is induced through exercise. Specifically, participants remained in a dry sauna maintained at 70 °C for 30 minutes to stimulate sweat secretion. As shown in Fig. 5c, valves 1, 3, and 5 are selectively actuated in sequence to demonstrate spatiotemporal targeting of sweat collection. Valve 1 is located at the top center of the circular layout, and valves are numbered counterclockwise. In a representative test, valve 1 is opened to collect sweat, then mechanically closed to transfer the contents to the collection chamber. This process is repeated for valves 3 and 5. Sweat accumulates only in the targeted chambers, with no observable leakage or mixing in
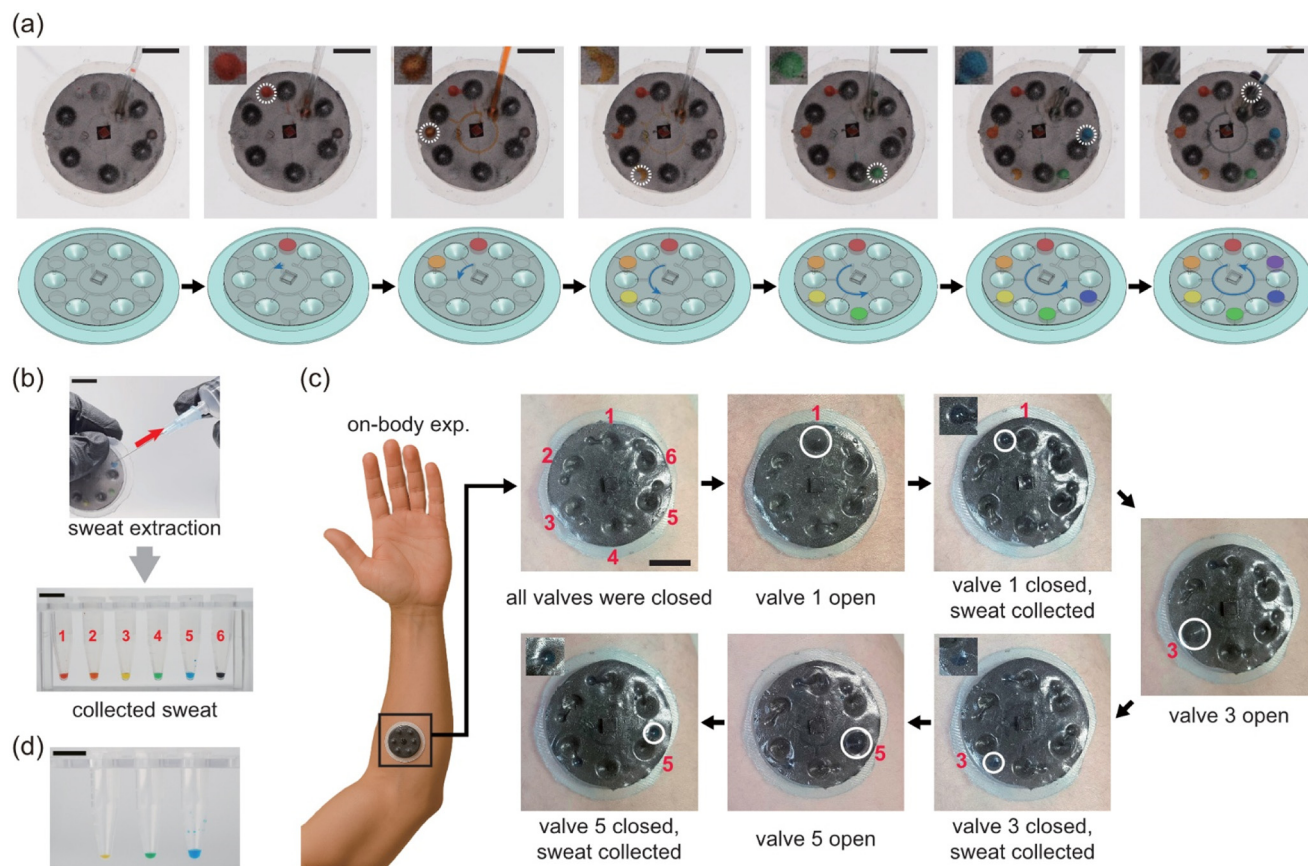
assists the snapping direction (positive current), the valve opens more readily, resulting in earlier leakage. For instance, under a 10 mbar inlet pressure, the valve remains closed for nearly 5 minutes without a magnetic field, withstands even longer when a negative field is applied, but opens significantly earlier with a positive field. These observations highlight the ability to control the valve's opening pressure by simply tuning the direction and magnitude of the external magnetic field. This magnetic tunability offers a practical advantage in wearable systems, where programmable fluid routing and adaptive actuation are highly desirable.

4.3 Reprogrammable collection in the sweat sampling device

We implement a sweat collection device that enables selective liquid collection into desired chambers using

Fig. 5 Reprogrammable and selective sweat collection using magneto-active bistable valves. (a) Bench-top demonstration of selective fluid routing: liquid is guided into a specific chamber by opening the corresponding valve with a magnet, while other chambers remain closed. (b) Collected sweat is retrieved by inserting a needle into the designated chamber and applying suction. The numbers indicate the sequential labeling of the collection chambers. (c) On-body demonstration with the sweat collection device attached to the inner forearm. Valves 1, 3, and 5 are actuated in sequence to collect sweat into targeted chambers. Valves are numbered counterclockwise starting from the top. Each chamber was filled to its full capacity of 22 μL, demonstrating consistent and complete fluid collection. (d) Demonstration of sweat collection at different volumes: 5 μL (yellow), 10 μL (green), and 20 μL (blue). All scale bars represent 10 mm.

other regions, confirming precise spatiotemporal control of sweat collection on skin, consistent with *in vitro* demonstrations.

To illustrate the system's ability to accommodate sweat collection at varying volumes, Fig. 5d presents representative cases with submaximal fluid amounts. This result confirms that collection can occur before the valve chamber is fully filled, enabling user-defined sampling intervals and supporting improved temporal resolution without altering chamber design.

5 Conclusion

We developed a wearable sweat collection device that integrates magneto-active bistable valves to achieve selective, chamber-specific fluid routing with minimal power requirements. Each valve toggles between stable open and closed states through magnetic actuation and mechanical indentation, eliminating the need for continuous energy input. This bistable architecture not only ensures energy-efficient operation but also enables

stable retention of valve states under dynamic on-body conditions.

Through both benchtop and on-body experiments, we demonstrated that the system effectively prevents sweat mixing across collection cycles, enabling precise spatiotemporal control over sweat sampling. Notably, the direction and strength of the applied magnetic field allowed programmable tuning of the valve's leaking pressure, providing real-time control over opening thresholds. This tunability represents a key advantage over conventional passive systems, which lack timing selectivity and are prone to cross-contamination.

Importantly, the selective gating mechanism introduced here enables discrete and contamination-free sampling in fully passive microfluidic formats. The modular design and wireless control architecture make the platform adaptable to various wearable biosensing applications, including multiplexed or location-specific biomarker monitoring. By embedding dynamically programmable control into skin-compatible microfluidics, this work offers a practical and scalable strategy for next-generation wearable diagnostics.

Data availability

The data supporting this article have been included as part of the ESI.†

Conflicts of interest

There are no conflicts to declare.

Acknowledgements

References

1 Q. Shi, Y. Yang, Z. Sun and C. Lee, *ACS Mater. Au*, 2022, **2**, 394–435.

2 L. Lu, J. Zhang, Y. Xie, F. Gao, S. Xu, X. Wu and Z. Ye, *JMIR Mhealth Uhealth*, 2020, **8**, e18907.

3 K. Guk, G. Han, J. Lim, K. Jeong, T. Kang, E. K. Lim and J. Jung, *Nanomaterials*, 2019, **9**, 813.

4 Z. Wang, J. Shin, J. H. Park, H. Lee, D. H. Kim and H. Liu, *Adv. Funct. Mater.*, 2021, **31**, 2008130.

5 F. Gao, C. Liu, L. Zhang, T. Liu, Z. Wang, Z. Song and N. Xue, *Microsyst. Nanoeng.*, 2023, **9**, 1.

6 G. Assalve, P. Lunetti, A. Di Cagno, E. W. De Luca, S. Aldegheri, V. Zara and A. Ferramosca, *Biosensors*, 2024, **14**, 574.

7 W. Gao, S. Emaminejad, H. Y. Y. Nyein, S. Challa, K. Chen, A. Peck and A. Javey, *Nature*, 2016, **529**, 509–514.

8 N. R. Jalal, T. Madrakian, M. Ahmadi, A. Afkhami, S. Khalili, M. Bahrami and M. Roshanaei, *Sci. Rep.*, 2024, **14**, 11526.

9 M. Yang, N. Sun, X. Lai, Y. Li, X. Zhao, J. Wu and W. Zhou, *Micromachines*, 2023, **14**, 1497.

10 I. Shitanda, N. Muramatsu, R. Kimura, N. Takahashi, K. Watanabe, H. Matsui and M. Itagaki, *ACS Sens.*, 2023, **8**, 2889–2895.

11 K. M. Clark and T. R. Ray, *ACS Sens.*, 2023, **8**, 3606–3622.

12 B. Ma, J. Chi, C. Xu, Y. Ni, C. Zhao and H. Liu, *Talanta*, 2020, **212**, 120786.

13 H. Zhao, X. Zhang, Y. Qin, Y. Xia, X. Xu, X. Sun and Q. Zhang, *Adv. Funct. Mater.*, 2023, **33**, 2212083.

14 L. Fiore, V. Mazzaracchio, A. Antinucci, R. Ferrara, T. Sciarra, F. Lista and F. Arduini, *Microchim. Acta*, 2024, **191**, 580.

15 H. Tabasum, N. Gill, R. Mishra and S. Lone, *RSC Adv.*, 2022, **12**, 8691–8707.

16 S. Jo, D. Sung, S. Kim and J. Koo, *Biomed. Eng. Lett.*, 2021, **11**, 117–129.

17 W. Li, E. W. K. Young, M. Seo, Z. Nie, P. Garstecki, B. A. Simmons and E. Kumacheva, *Langmuir*, 2007, **23**, 8010–8014.

18 D. J. O'Brien, S. A. Hill, J. S. Horwitz, N. Novikova, X. Lin and B. N. Johnson, *J. Microelectromech. Syst.*, 2020, **29**, 1216–1224.

19 P. Rothemund, A. Ainla, L. Belding, D. J. Preston, S. Kurihara, Z. Suo and G. M. Whitesides, *Sci. Robot.*, 2018, **3**, eaar7986.

20 A. Pal and M. Sitti, *Proc. Natl. Acad. Sci. U. S. A.*, 2023, **120**, e2212489120.

21 W. Gao, S. Emaminejad, H. Y. Y. Nyein, S. Challa, K. Chen, H. Ota, H. M. Fahad and A. Javey, *Adv. Healthcare Mater.*, 2017, **6**, 1601355.

22 W. He, W. Gao, H. Y. Y. Nyein, H. Ota, S. Challa, A. Peck, H. M. Fahad, D. Kiriya, K. Chen and A. Javey, *Small*, 2018, **14**, 1703334.

23 J. Choi, D. Kang, S. H. Han, S. B. Kim and J. A. Rogers, *Adv. Healthcare Mater.*, 2017, **6**, 1601355.

24 S. B. Kim, J. Choi, D. Kang, S. H. Han and J. A. Rogers, *Small*, 2018, **14**, 1703334.

25 N. F. A. Ibrahim, S. Salleh, S. F. Shaarani, M. F. F. Zawawi and N. A. Yusof, *Sensors*, 2022, **22**, 7670.

26 W. Wang, Y. Jin, Y. Huang, Z. Zhao, M. Li, H. Mao and J. Xiong, *Sens. Actuators, B*, 2024, **414**, 135920.

27 S. Shajari, R. Salahandish, A. Zare, M. Hassani, S. Moossavi, E. Munro and A. Sanati Nezhad, *Adv. Sci.*, 2023, **10**, 2204171.

28 J. T. Reeder, Y. Xue, D. Franklin, Y. Deng, J. Choi, O. Prado, R. Kim, C. Liu, J. Hanson and J. Ciraldo, *Nat. Commun.*, 2019, **10**, 5513.

29 M. Bariya, N. Davis, L. Gillan, E. Jansson, A. Kokkonen, C. Mc-Caffrey, J. Hiltunen and A. Javey, *ACS Sens.*, 2022, **7**, 1156–1164.

30 N. Mishra, N. T. Garland, K. A. Hewett, M. Shamsi, M. D. Dickey and A. J. Bandodkar, *ACS Sens.*, 2022, **7**, 3169–3180.

31 M. I. H. Gama, S. Abdullahi, M. O. M. Omer, Z. Yang, X. Wang, Y. B. M. Osman, Y. Liu, J. Li, Y. Li and X. Gao, *Lab Chip*, 2025, **25**, 3094–3108.

32 M. Brinkmeyer, A. Brinkmeyer, D. Yang and J. L. Silverberg, *Nat. Commun.*, 2022, **13**, 1078.

33 D. P. Holmes and A. J. Crosby, *Adv. Mater.*, 2010, **19**, 3582–3586.

34 H. Liang and L. Mahadevan, *Proc. R. Soc. A*, 2011, **467**, 3025–3044.

35 S. Shan, S. H. Kang, J. R. Raney, P. Wang, L. Fang and K. Bertoldi, *Adv. Mater.*, 2015, **27**, 4296–4301.

36 A. Abbasi, T. Chen, B. F. Aymon and P. M. Reis, *Adv. Mater. Technol.*, 2024, **9**, 2301344.

37 M. Zrínyi, L. Barsi and D. Szabó, *J. Chem. Phys.*, 1996, **104**, 8750–8756.

38 G. Filipcsei, I. Csetneki, A. Szilágyi and M. Zrínyi, *Adv. Polym. Sci.*, 2007, **206**, 137–189.

39 Y. Li, J. Li, P. Zhang, G. Huang, X. Ruan, B. Yang and T. Wang, *Adv. Funct. Mater.*, 2014, **24**, 4601–4610.

40 A. J. Bandodkar, I. Jeerapan and J. Wang, *Sci. Adv.*, 2016, **2**, e1601465.

41 L. Dong, Y. Qi, L. Liu, W. Li and H. Du, *Adv. Mater.*, 2013, **25**, 5961–5965.

42 H. Yang, X. Gong, C. Yang and X. Zhao, *ACS Appl. Mater. Interfaces*, 2016, **8**, 27432–27438.

43 R. E. Rosensweig, *Ferrohydrodynamics*, Cambridge University Press, 1985.

44 Y. Kim, H. Yuk, R. Zhao, S. A. Chester and X. Zhao, *Adv. Mater.*, 2020, **32**, 2003150.